Mon. Not. R. astr. Soc. (1992) **255**, 561–571

Self-consistent two-component models of elliptical galaxies

L. Ciotti and S. Pellegrini
Dipartimento di Astronomia, Università di Bologna, via Zamboni 33, 40126 Bologna, Italy

Accepted 1991 November 4. Received 1991 September 30; in original form 1991 July 10

SUMMARY

Spherical self-consistent elliptical galaxy models, embedded in a dark matter halo, are constructed. Two different stellar distributions are considered: the King law, and another one reproducing the $R^{1/4}$ luminosity law; the stellar mass-to-light ratio is constant. The concentration and the amount of the stellar and dark matter distributions are determined by five parameters; two characteristic radii determine the radial trend of the anisotropy for the stellar and dark halo velocity dispersion tensors. We introduce the multicomponent decomposition of dynamical models of galaxies, and a theorem concerning their consistency; then, we determine the region of the parameter space where the models are self-consistently generated. For some models lying in this region the stellar velocity dispersion profiles are described in detail, pointing out the effects of the anisotropy and of the dark matter. We also show the errors induced by these effects on the results of the most common methods of elliptical galaxies' mass estimation. We finally discuss the reduction produced by the so-called *fundamental plane* in the number of independent parameters, and their role in the energetics of hot gas flows in ellipticals.

1 INTRODUCTION

The observed surface brightness distribution of elliptical galaxies can be well fitted by the King law (King 1962, 1966) or by the de Vaucouleurs law (de Vaucouleurs 1948). In this paper we present both types of galaxy model, embedded in a dark matter halo, and with various amounts of anisotropy in the stellar and dark matter velocity dispersion tensors. The main assumptions are the following: (i) the galaxies are spherically symmetric, in equilibrium, and fully pressure-supported; (ii) the stellar mass-to-light ratio is constant, and (iii) radial anisotropy in the velocity dispersion tensor is permitted. The assumption of spherical symmetry may be wrong for a large fraction of ellipticals, so our results can be considered fairly appropriate for galaxies with quite round isophotes and very little rotation.

Non-luminous mass may exist in elliptical galaxies in several forms, and an increasing body of evidence requires the presence of a large component of dark matter: see for example *Einstein* X-ray observations of hot gaseous coronae around ellipticals (Forman, Jones & Tucker 1985), or HI observations of ellipticals with cold gas (Lees, van Gorkom & Knapp 1990). Extensive searches for dynamical evidence of dark matter are underway, through systematic observations of warm gas probing the gravitational field (Bertola *et al.* 1991), or measurements of stellar velocity dispersion profiles (Bertin *et al.* 1989). The results of these latter studies are restricted to the region inside two half-light radii.

The importance of taking into account an anisotropic stellar velocity dispersion tensor comes from the fact that radial anisotropy is expected in ellipticals that form via collisionless collapse (van Albada 1982). We are not aware of specific indications about the anisotropy in the dark component, so we explore various degrees of radial anisotropy for it.

The above considerations induced us to address the following three general topics. We first investigate whether anisotropic two-component galaxy models such as those we construct can be self-consistently generated. The results of this investigation are explained with the aid of a new theorem concerning the necessary and a sufficient condition on the density profiles and the radial trends of the anisotropy. This theorem holds in the general case of multicomponent galaxy models with the adopted velocity dispersion tensor. Then we compute from the Jeans equation the spatial and projected stellar velocity dispersion profiles of the most characteristic self-consistent models. Next we turn to a classic problem in the dynamics of elliptical galaxies: the determination of masses from observed velocity dispersions. We integrate the stellar velocity dispersion profiles over apertures centred on the model galaxies in order to determine whether the most common mass estimators are able to give reliable estimates of the total or of the stellar mass, if stellar anisotropy or dark matter are present.

In previous works, stellar velocity dispersions against radius have been given for one-component models: Bailey &

© Royal Astronomical Society • Provided by the NASA Astrophysics Data System

MacDonald (1981) studied King and de Vaucouleurs isotropic models, and Tonry (1983) studied anisotropic velocity dispersions in de Vaucouleurs spherical galaxy models. The error in the estimate of the central stellar mass-to-light ratio with the core-fitting formula, due to anisotropy, was studied by Merritt (1988) and Richstone & Tremaine (1984). Mathews (1988) tested the sensitivity to the presence of dark matter and non-isotropic stellar velocity ellipsoids of observational procedures used to determine the mass-to-light ratio, without investigating the physical consistency of his models. A first, extensive survey of two-component, spherical, self-consistent galaxy models was carried out by Bertin, Saglia & Stiavelli (1991). They assume, for the stellar and dark matter components, two parametrized distribution functions of the f_∞ form (Bertin & Stiavelli 1984).

In Section 2 we describe our King and de Vaucouleurs galaxy models, in Section 3 we present the stellar velocity dispersion profiles, in Section 4 we study the self-consistency of our models and in Section 5 we treat the problem of obtaining galaxy masses from mass estimators. In Section 6 we discuss how the so-called *fundamental plane* constrains the parameter space, and we calculate some physical quantities useful for the study of hot gas flows in ellipticals. Finally, in Section 7 we summarize the results.

2 THE MODELS

We consider two distinct classes of two-component spherical galaxy models, in which the stellar (bright matter) density distribution is described by the analytical fit of the King law, or by the $R^{1/4}$ law, when projected. Both models are embedded in a dark matter distribution (DH). The *stellar* mass-to-light ratio (M_*/L_B) is kept constant through all the galaxy, and so the luminosity profile can be recovered immediately from the stellar mass distribution. Throughout the paper we indicate with r the spatial radius and with R the projected radius of the galaxy models.

2.1 King model galaxies

For a first group of models that we call King Galaxies (KGs) we assume the stellar distribution to be described by the density profile:

$$\rho_*(r) = \frac{\rho_{*o}}{(1+r^2/r_{c*}^2)^{3/2}}, \tag{1}$$

where r_{c*} and ρ_{*o} are respectively the core radius and the central stellar density of the galaxy (King 1972). This distribution is truncated at the tidal radius r_t. The density law in (1) is exempt from central singularities, allows for a complete analytical treatment of quantities such as the gravitational potential and force, and gives optical surface brightness profiles in reasonable agreement with those of many ellipticals (Kormendy 1987). The surface brightness profile $I_K(R)$ is given by $I_K(R)=(M_*/L_B)^{-1}\Sigma_K(R)$, where $\Sigma_K(R)$ is the projected mass distribution derived from (1):

$$\Sigma_K(R) = \frac{2\rho_{*o}r_{c*}^3}{\sqrt{r_t^2+r_{c*}^2}}\,\frac{\sqrt{r_t^2-R^2}}{r_{c*}^2+R^2}. \tag{2}$$

In Fig. 1 we show $\Sigma_K(R)$ for $r_t = 140\,r_{c*}$. For $r_t \to \infty$, (2) gives the modified Hubble profile (e.g. Binney & Tremaine 1987, hereafter BT87). For KGs we assume the DH density profile to follow a quasi-isothermal law:

$$\rho_h(r) = \frac{\rho_{ho}}{1+r^2/r_{ch}^2}, \tag{3}$$

where r_{ch} is a scale radius, ρ_{ho} is the central density, and the tidal radius is assumed to be the same as for the stars. The DH projected mass profile is

$$\Sigma_h(R) = 2\rho_{ho}r_{ch}^2\,\frac{\arctan\sqrt{(r_t^2-R^2)/(r_{ch}^2+R^2)}}{\sqrt{r_{ch}^2+R^2}}. \tag{4}$$

The total stellar mass, the total DH mass, and the total mass of the system are respectively $M_* = M_*(r_t)$, $M_h = M_h(r_t)$ and $M_T = M_* + M_h$. This notation will be applied also to the de Vaucouleurs model galaxies to be introduced below. Then KGs are fully determined by fixing five independent parameters: we choose $(M_*, r_{c*}, M_h, r_{ch}, r_t)$.

We plot in Fig. 2 the ratio $M_T(r)/M_*(r)$ for two different values of r_{ch}/r_{c*} and M_h/M_*. The value of r_{ch}/r_{c*} is crucial in keeping the total mass distribution close to that of the stars in the central regions of the galaxy: large values force most of the dark mass to lie in the external regions.

2.2 de Vaucouleurs model galaxies

The second class of models we consider (dVGs) is composed of a stellar distribution that reproduces the de Vaucouleurs law, when projected, and of a DH described by the same mass distribution, but with different physical scales. We have modelled the stellar density profile using the approximation given by Mellier & Mathez (1987):

$$\rho_*(r) = \rho_{*o}(b^4 r/R_{e*})^{-0.855}\exp[-b(r/R_{e*})^{0.25}], \tag{5}$$

where $b = 7.66925$ and R_{e*} is the effective radius; for the DH, R_{e*} is replaced by R_{eh} and ρ_{*o} by ρ_{ho}. As in the case of KGs, we truncate the dark and the luminous distributions at a common tidal radius r_t. Notwithstanding the introduction of a tidal radius, the projection of (5), $\Sigma_{MM}(R)$, keeps close to the projected mass distribution corresponding to the $R^{1/4}$ law, $\Sigma_{dV}(R)$, over the major fraction of the galaxy. This quantity is written (Mellier & Mathez 1987):

$$\Sigma_{dV}(R) = \frac{2\rho_{*o}R_{e*}}{b^4\Gamma(8)/\Gamma(8.58)}\exp[-b(R/R_{e*})^{0.25}]. \tag{6}$$

The deviations of $\Sigma_{MM}(R)$ from $\Sigma_{dV}(R)$ are reported in Fig. 1, for $r_t = 15\,R_{e*}$: the drop below the solid line at large radii is due to the presence of the tidal radius, and the central raising is due to the steeper divergence of (5) with respect to the de Vaucouleurs density profile, that diverges as $r^{-3/4}$ (Young 1976).

In analogy with KGs, dVGs are uniquely determined by assigning five independent parameters, which we choose as $(M_*, R_{e*}, M_h, R_{ch}, r_t)$. We show, in Fig. 2, $M_T(r)/M_*(r)$ for two values of R_{ch}/R_{e*} and M_h/M_*: the same comments as for KGs apply, with the difference that in this case a large fraction of dark mass is always present within the central regions, even for large values of R_{eh}/R_{e*}, because the stellar and DH distributions have the same divergent behaviour in the centre. If $R_{e*} = R_{eh}$ the DH has the same density

© Royal Astronomical Society • Provided by the NASA Astrophysics Data System

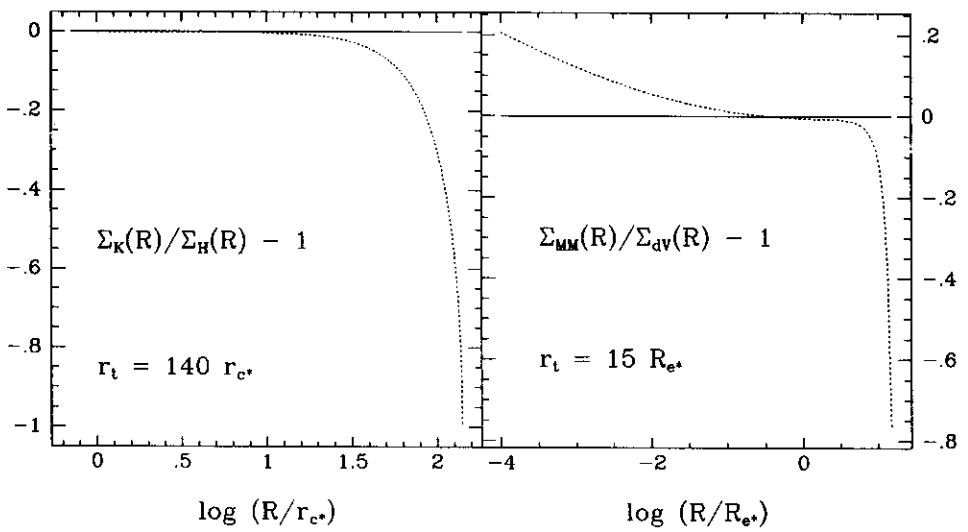

Figure 1. Left panel: the dotted line represents the deviation of the projection $\Sigma_K(R)$ from the modified Hubble profile, $\Sigma_H(R)$. Right panel: the deviation of $\Sigma_{MM}(R)$ from the de Vaucouleurs profile, $\Sigma_{dV}(R)$.

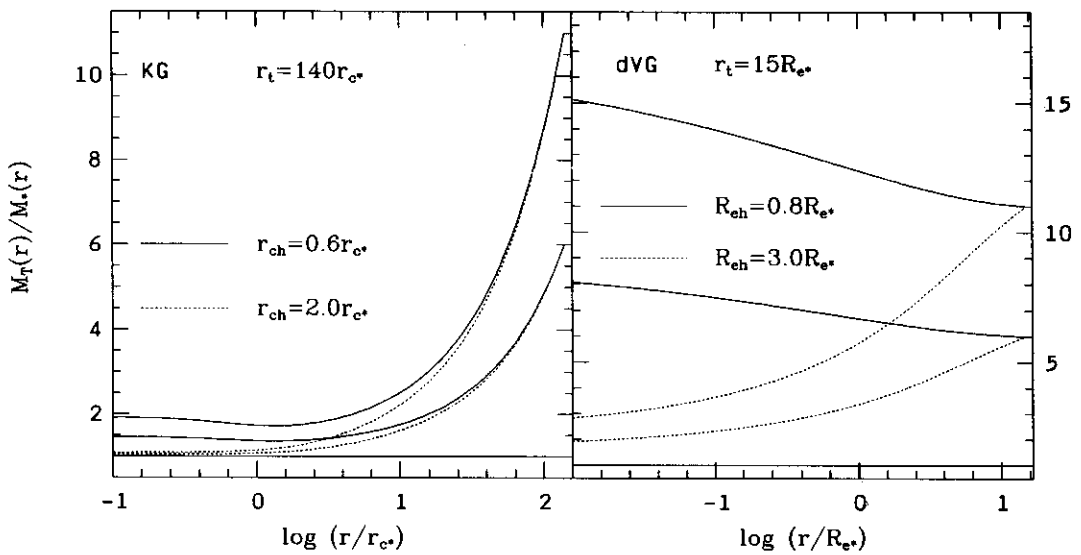

Figure 2. The ratio $M_T(r)/M_*(r)$ for KGs (left panel) and for dVGs (right panel). The straight solid line represents a model with no DH; for the other lines $M_h = 5M_*$ and $10M_*$.

profile as the luminous matter all over the galaxy, and $M_h(r)/M_*(r) = M_h/M_*$.

3 SPATIAL AND LINE-OF-SIGHT VELOCITY DISPERSION PROFILES

In this section we present the spatial and line-of-sight velocity dispersion profiles for the stellar component, in the cases of isotropic or anisotropic velocity dispersion tensors, and with various amounts and distributions of dark matter. For spherical anisotropic models, the only distinct components of the velocity dispersion tensor are $\sigma_r^2(r)$ and $\sigma_\theta^2(r)$, with $\sigma_\theta^2(r) = \sigma_\phi^2(r)$, so that the total velocity dispersion is $\sigma^2(r) = \sigma_r^2(r) + 2\sigma_\theta^2(r)$. In order to obtain the radial component $\sigma_r^2(r)$, we integrate the Jeans equation:

$$\frac{1}{\rho_*(r)}\frac{d\rho_*(r)\sigma_r^2(r)}{dr} + 2\frac{\alpha_*(r)\sigma_r^2(r)}{r} = -\frac{d\phi(r)}{dr}, \tag{7}$$

where $\phi(r) = \phi_*(r) + \phi_h(r)$ is the total potential, and $\alpha_*(r) = 1 - \sigma_\theta^2(r)/\sigma_r^2(r)$. The line-of-sight velocity dispersion profile $\sigma_p^2(R)$ is then recovered by integrating the following expression:

$$\Sigma_*(R)\sigma_p^2(R) = 2\int_R^{r_t}\left[1 - \alpha_*(r)\frac{R^2}{r^2}\right]\frac{\rho_*(r)\sigma_r^2(r)\,r\,dr}{\sqrt{r^2 - R^2}} \tag{8}$$

(Binney & Mamon 1982). An equation similar to (7) holds for the velocity dispersion of the DH component, with $\alpha_*(r)$ and $\rho_*(r)$ replaced by $\alpha_h(r)$ and $\rho_h(r)$.

© Royal Astronomical Society • Provided by the NASA Astrophysics Data System

There are some conditions which $\alpha_*(r)$ has to obey: N-body simulations of collisionless collapses (e.g. van Albada 1982) show the prevalence of radial anisotropic orbits in the outer parts of elliptical galaxies, while in the central regions the velocity dispersion tensor is highly isotropic. So, numerical models of galaxies suggest that $\sigma_r^2(r) \geq \sigma_\theta^2(r)$ at any radius, i.e. $0 \leq \alpha_*(r) \leq 1$, with $\alpha_*(r)$ an increasing function of r. Given these assumptions, we adopt $\alpha_*(r) = r^2/(r^2 + r_{a*}^2)$ [and $\alpha_h(r) = r^2/(r^2 + r_{ah}^2)$], and the integration of (7) is performed using the quadrature formula given by Binney (1980); the boundary condition is $\rho_*(r_t)\sigma_r^2(r_t) = 0$. In all these models isotropy is realized in the galaxy centre; only in the limits $r_{a*} \to \infty$, $\alpha_*(r) = 0$, i.e. the component has an entirely isotropic velocity dispersion tensor.

3.1 Velocity dispersion profiles of KGs and dVGs

First we discuss the radial, projected, and total velocity dispersion profiles of KGs. To give some insights into the effects of the parameters, we choose their values as $r_{a*} = \infty$ and $12r_{c*}$; $M_h = 0$ and $10M_*$; $r_{ch} = 0.6r_{c*}$ and $2r_{c*}$; r_t is fixed at $140r_{c*}$.

In Fig. 3(a) we plot $\sigma_r(r)/\sqrt{G\rho_{*0}r_{c*}^2}$ (G is the gravitational constant). Several features are apparent as r_{ch}/r_{c*}, M_h/M_* and r_{a*}/r_{c*} vary. All KGs show a flat $\sigma_r(r)$ in the central regions of the galaxy. For models *with no* DH and large values of r_{a*}/r_{c*}, the central profile almost coincides with the (constant) value proper of the isothermal sphere, $\sigma_{is}/\sqrt{G\rho_{*0}r_{c*}^2} = \sqrt{4\pi/9}$ (cgs units). Decreasing the value of r_{a*}/r_{c*} makes the whole profile higher (see, e.g., Tonry 1983) in KGs with or without DH: this effect is most evident for the profile with $r_{a*} = 3.5r_{c*}$, referring to a model with no DH. Not only the stellar anisotropy is responsible for an increase of the central velocity dispersion profile, but also the DH. Its concentration acts in the sense that the smaller the value of r_{ch}/r_{c*}, the higher $\sigma_r(0)$ becomes, because more mass is present in the central regions (see Fig. 2). In the outer parts also, the main effect of the DH is to increase $\sigma_r(r)$. For isotropic models, this results in quite flat profiles. Consistently with our choice of the radial trend of the anisotropy, the anisotropic $\sigma_r(r)$s are higher than the isotropic ones.

In Fig. 3(b) we plot $\sigma_p(R)\sqrt{G\rho_{*0}r_{c*}^2}$. At small radii the behaviour is qualitatively the same as that of the corresponding $\sigma_r(r)$. In the external part there is a large reduction in the anisotropic profiles, due to the prevalence of orbits perpendicular to the line of sight: this reduction causes the anisotropic model's profile to be lower than that of the isotropic one. The projection effect is also responsible for the slight increase of each $\sigma_p(r)$ with respect to the corresponding $\sigma_r(r)$ in the centre, as already pointed out by Tonry (1983) and by BT87 (p. 242). From an observational point of view, it is interesting to note that when a DH is present, $\sigma_p(R)$ keeps flat out to many r_{c*}, if $r_{a*} = \infty$, but otherwise $\sigma_p(R)$ drops even faster than in models with no DH. In Fig. 3(c) the total velocity dispersion is plotted. The lower straight solid line is the virial velocity dispersion value, for all the models with no DH; it is somewhat lower than $\sigma_{is}\sqrt{3}$, because of the introduction of the tidal radius r_t.

The radial, projected, and total velocity dispersion profiles of dVGs are plotted in Fig. 4. We choose $r_{a*} = \infty$ and R_{e*}; $M_h = 0$ and $10M_*$; $R_{eh} = 0.8R_{e*}$ and $3R_{e*}$; $r_t = 15R_{e*}$. In Fig. 4(a), dVGs *with no* DH (solid lines) show the well-known drop of $\sigma_r(r)$ at small radii; the maximum is reached at $0.08R_{e*}$ for isotropic models. The virial velocity dispersion value is virtually the same as that of a pure de Vaucouleurs model, which is equal to $1.5 \times 10^{-3}\sqrt{G\rho_{*0}R_{e*}^2}$ (Poveda 1958). Again, in the external regions the anisotropic model profile is higher than the isotropic one. For dVGs *with* DH, the same comments as for KGs apply, with the difference that isotropic profiles are not flat, consistent with the shape of the potential well. A remarkable difference is also that, while in the central regions of KGs the anisotropy alone can make $\sigma_r(r)$ increase by the same amount as does the DH (even with $M_h = 10M_*$), for dVGs the DH is much more effective than the stellar anisotropy.

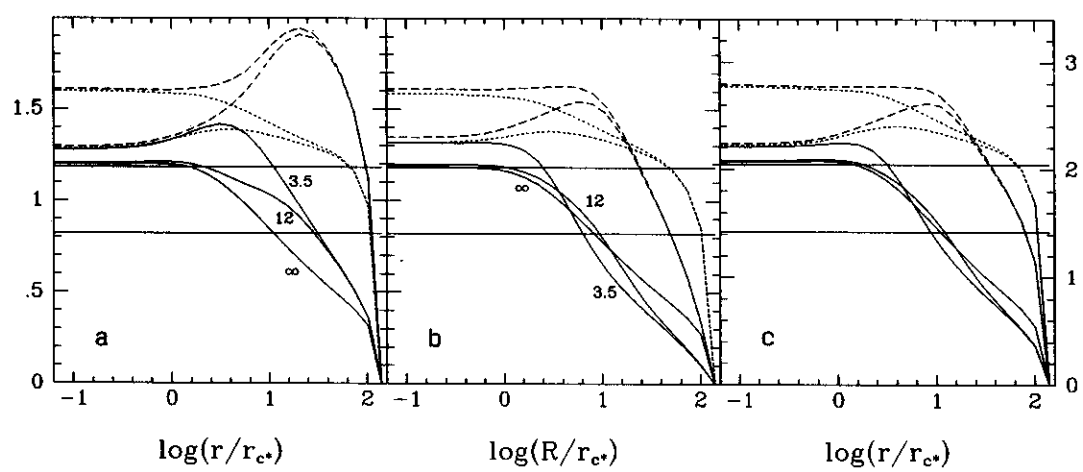

Figure 3. The radial (a), projected (b) and total (c) velocity dispersion profiles for KGs, normalized to $\sqrt{G\rho_{*0}r_{c*}^2}$. The straight solid lines are the value of $\sqrt{4\pi/9}$ (isothermal sphere), and the virial velocity dispersion value for KGs with no DH (lower line). In each panel the solid curves refer to models with no DH (the numbers give the value of r_{a*}/r_{c*}), and the others to KGs with $M_h = 10M_*$: the dotted lines are isotropic models with $r_{ch} = 0.6r_{c*}$ (higher curve) or $r_{ch} = 2r_{c*}$, and the dashed lines are anisotropic models ($r_{a*} = 12r_{c*}$) with $r_{ch} = 0.6r_{c*}$ (higher curve) or $r_{ch} = 2r_{c*}$.

© Royal Astronomical Society • Provided by the NASA Astrophysics Data System

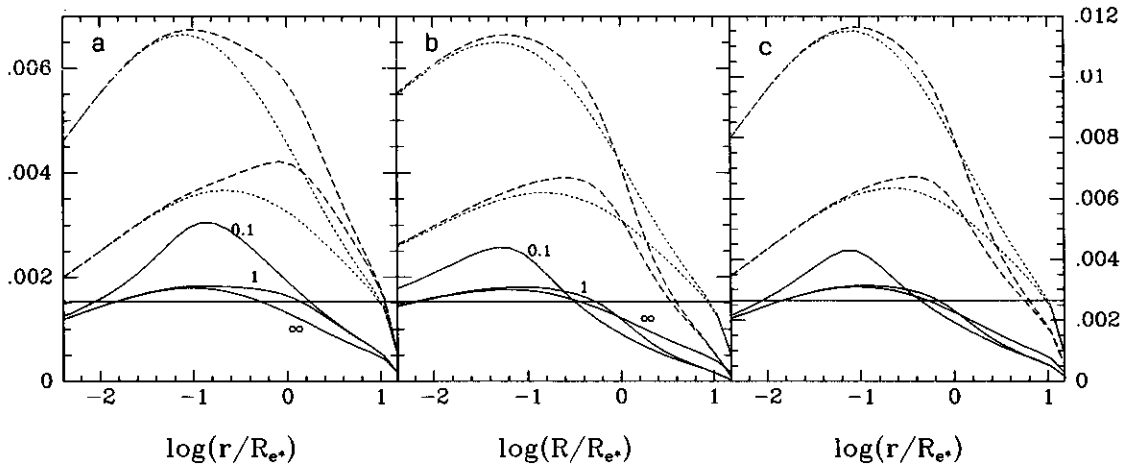

Figure 4. The radial (a), projected (b) and total (c) velocity dispersion profiles for dVGs, normalized to $\sqrt{G\rho_{*0}R_{e*}^2}$. The straight solid line is the value of the virial velocity dispersion for dVGs with no DH. In each panel the solid profiles refer to models with no DH (the numbers give the value of r_{a*}/R_{e*}), and the others to dVGs with $M_h = 10M_*$: the dotted lines are isotropic models with $R_{ch} = 0.8R_{e*}$ (higher curve) or $R_{ch} = 3R_{e*}$, and the dashed lines are anisotropic models ($r_{a*} = R_{e*}$) with $R_{ch} = 0.8R_{e*}$ (higher curve) or $R_{ch} = 3R_{e*}$.

Fig. 4(b) shows that $\sigma_p(R)$ decreases at large radii independently of the presence of the DH; the ratio of the maximum of σ_p to a characteristic value [for example $\sigma_p(R_{e*})$], for constant M_h/M_*, is clearly dependent on R_{ch}/R_{e*}.

4 THE CONSISTENCY OF MULTICOMPONENT GALAXY MODELS

As important as the construction of its spatial and projected velocity dispersion profile is to check whether a model is dynamically consistent. In order to investigate this problem, we first introduce some nomenclature holding in general cases, then we concentrate on specific models in which each component has a velocity dispersion tensor as described in Section 3. Lastly, we give a theorem enlightening the roles of the densities, total potential, and anisotropies in making a model unphysical.

Any collisionless system subject to a potential ϕ is completely described by its phase-space distribution function, $f = f(\boldsymbol{x}, \boldsymbol{v}; t)$, satisfying the collisionless Boltzmann equation $\partial f/\partial t + B(f, \phi) = 0$ (see, e.g. BT87, p. 190). This function is the probability density of finding some star in the volume $d^3\boldsymbol{x}d^3\boldsymbol{v}$ centred on $(\boldsymbol{x}, \boldsymbol{v})$ at the time t, so it must be nowhere negative. We call *consistently generated* any system derived from a non-negative distribution function. If, moreover, the density is related to the total potential ϕ by the Poisson equation, the system is called *self-consistently generated*. In the stationary case, f depends on $(\boldsymbol{x}, \boldsymbol{v})$ only through the integrals of motion of the system (Jeans Theorem); in the particular case of spherical symmetry without rotation, the only useful integrals are the specific total energy and the specific angular momentum modulus, so $f = f(E, L^2)$. We now introduce the multicomponent decomposition of a general stationary system.

Definition I

For a given $f(\boldsymbol{x}, \boldsymbol{v})$ for which $B(f, \phi) = 0$, $\int f d^3\boldsymbol{v} = \rho \geq 0$ and $\nabla^2\phi = 4\pi G\rho$, we define the multicomponent decomposition (MCD) of f as any set of $f_i (i = 1, \ldots, N)$ that satisfies $\Sigma_{i=1}^N f_i = f$, $B(f_i, \phi) = 0$ and $\int f_i d^3\boldsymbol{v} = \rho_i \geq 0$, for any i.

We note that, for any MCD, $\Sigma_{i=1}^N \rho_i = \rho$, and different MCDs can give the same set of ρ_i.

Definition II

We define the consistent multicomponent decomposition (CMCD) of f as any MCD of f for which $f_i \geq 0$ for any i.

It is straightforward to show that *a system is self-consistently generated* $\Leftrightarrow \exists$ *a CMCD for it*, and that in any CMCD the ρ_i are not self-consistently generated. Moreover, the various components of a dynamical system interact exclusively through the total potential, so the consistency of each one of them is independent of the anisotropy of the others. The MCD of our galaxy models is made up of f_* and f_h; so KGs and dVGs are self-consistently generated when f_* and f_h are both nowhere negative.

Thanks to our choice of the radial trend of the stellar and DH velocity dispersions, we are allowed to use particular forms for f_* and f_h that can be easily constructed. Following Merritt (1985), the distribution function of each ith component is:

$$f_i(Q_i) = \frac{1}{\sqrt{8\pi^2}} \frac{d}{dQ_i} \int_0^{Q_i} \frac{d\varrho_i}{d\Psi} \frac{d\Psi}{\sqrt{Q_i - \Psi}}, \tag{9}$$

where $\varrho_i = \rho_i \times (1 + r^2/r_{ai}^2)$, $\Psi(r) = -\phi(r) + \phi(r_t)$, $Q_i = \phi(r_t) - E - L^2/2r_{ai}^2$ and $0 \leq Q_i \leq \Psi(0)$. [Clearly the total system is not generated by an f such as that in (9), because its $\alpha(r)$ is not of the requested form, but is the pondered mean of each $\alpha_i(r)$ with the product of $\rho_i(r)$ and the square radial velocity dispersion of the ith component.] We are interested, not in deriving the specific form of the f_i from (9), but in its non-negativity. So, we have to test when the integral in (9) is a non-decreasing function of Q_i. This can be checked numerically, but here we give a theorem that enables us to make some predictions and, in particular, to explain the numerical results for our KGs and dVGs.

© Royal Astronomical Society • Provided by the NASA Astrophysics Data System

Theorem

The necessary condition for the non-negativity of $f_i(Q_i)$ given in (9) is $d\varrho_i/d\Psi \geq 0$. If, as usual, $\rho_i' = d\rho_i/dr \leq 0$, the necessary condition becomes:

$$1+\frac{r^2}{r_{ai}^2}+\frac{\rho_i(r)}{\rho_i'(r)}\frac{2r}{r_{ai}^2}\geq 0, \qquad \text{for } 0\leq r\leq r_t. \tag{10}$$

[This can be stated also by requiring that $\rho_i\times(r_{ai}^2+r^2)$ is a non-increasing function of r.] If this necessary condition is satisfied, a sufficient condition for the non-negativity of $f_i(Q_i)$ is that

$$\frac{d\varrho_i}{d\Psi}\sqrt{\Psi}=-\frac{r^2\rho_i'(r)}{GM_t(r)}\left[1+\frac{r^2}{r_{ai}^2}+\frac{\rho_i(r)}{\rho_i'(r)}\frac{2r}{r_{ai}^2}\right]\sqrt{\Psi(r)} \tag{11}$$

is a non-increasing function of r.

Proof

Let

$$I_g(Q)=\int_0^Q g(x)(Q-x)^{-1/2}\,dx,$$

with $0\leq Q\leq Q_0$. The necessary condition for $I_g(Q)' = dI_g(Q)/dQ \geq 0$ is $g(x)\geq 0$, for $0\leq x\leq Q_0$. In fact, recovering $g(x)$ from the Abel inversion, and using the condition $I_g(0)=0$, if $I_g(Q)'\geq 0$ we have also that $g(x)$ is non-negative for any value of x. The sufficient condition is proved as follows. After changing the integration variable to x/Q, and after the derivation of $I_g(Q)$ with respect to Q, the original variable is restored. So

$$I_g(Q)'\geq 0 \Leftrightarrow \int_0^Q [g(x)/2+xg(x)'](Q-x)^{-1/2}\,dx\geq 0,$$

for $0\leq Q\leq Q_0$. Then a sufficient condition for $I_g(Q)'\geq 0$ is given by the positivity of the integrand. If $g(x)\geq 0$, this condition reduces to the non-negativity of $d\ln[\sqrt{x}g(x)]/dx$, i.e. to $\sqrt{x}g(x)$ being a non-decreasing function of x. Setting $g(x)=d\varrho_i/d\Psi$ completes the proof.

4.1 Testing the consistency

Some considerations follow looking at the conditions (9)–(11). Two different ways exist of making one component unphysical. The first is the violation of the necessary condition in (10), and we call it *geometrical*, because it is connected only with the radial behaviour of ρ_i and the value of r_{ai}. It can be easily shown that one value of r_{ai} exists (in case ∞) such that all r_{ai}s smaller than this value make the component inconsistent, while for all the larger values, (10) is satisfied. For example, for the density profile in (3), the geometrical limit on the anisotropy is $r_{ah}\geq r_{ch}$, as can be found by direct application of (10); for the density profile in (1) it is $r_{a*}\geq\sqrt{2/3}r_{c*}\simeq 0.817r_{c*}$; for (5) it is $r_{a*}\geq 0.02R_{e*}$. When $\rho\propto r^{-\nu}$, and $\nu\geq 2$, any anisotropy radius is permitted (see also Richstone & Tremaine 1984).

Even when the necessary condition (10) is satisfied, f_i can be negative, due to the radial behaviour of the integrand in (9), which depends on the total potential, on the particular ρ_i, and finally on r_{ai}. We call *dynamical* this way of making a model unphysical. So, some permitted values of r_{ai} satisfying the geometrical requirement must be discarded. Naturally, the value of the dynamical limit on anisotropy is always larger than or equal to that of the geometrical one, and smaller than or equal to that given by the sufficient condition (11). For example, in the case of (1), the dynamical limit derived numerically is $r_{a*}\geq 0.896r_{c*}$, while the sufficient condition is $r_{a*}\geq 0.927r_{c*}$. Numerical calculations show that the dynamical limit for the density profile in (5) is $r_{a*}\geq 0.05R_{c*}$, as Merritt (1985) found for de Vaucouleurs stellar models.

An important result follows for a particular class of two-component models: a stellar density profile such as that in (5) cannot be consistently coupled to a DH as given in (3). In fact, unless very small values of $r_{ch}/R_{e*}(<10^{-3})$ are assumed, $f_h<0$; this limit is almost independent of the value of r_{ah}/r_{ch}, and holds also in the isotropic case. The dynamical inconsistency is due to (3) being too flat at small radii with respect to the central divergence of the stellar density producing the de Vaucouleurs law. So, in our opinion, a lot of caution is necessary in interpreting the results of Mathews (1988).

We discuss now the numerical results giving the region of parameter space where KGs and dVGs are self-consistently generated. These results are shown for KGs in Fig. 5: the dot-dashed line marks the upper boundary of the region of non-negativity of f_h, and the dotted lines the lower boundary of the region where f_* is non-negative. The non-negativity of f_h is obtained for $r_{ah}>r_{ch}$ and for $r_{ch}\lesssim 2.2r_{c*}$, as $0\leq M_h\leq 10M_*$. This is clearly a dynamical limit: for larger r_{ch}/r_{c*}, the DH density profile in the central parts of the model is too flat to be compatible with the stellar profile. This same dynamical effect makes f_* negative for the smallest values of r_{ch}/r_{c*}, so the consistency of the stellar component is assured for $r_{ch}\geq 0.3r_{c*}$ and $r_{a*}>0.896r_{c*}$. The lower limit on r_{ch}/r_{c*} increases slightly, decreasing r_{a*} and increasing M_h/M_*.

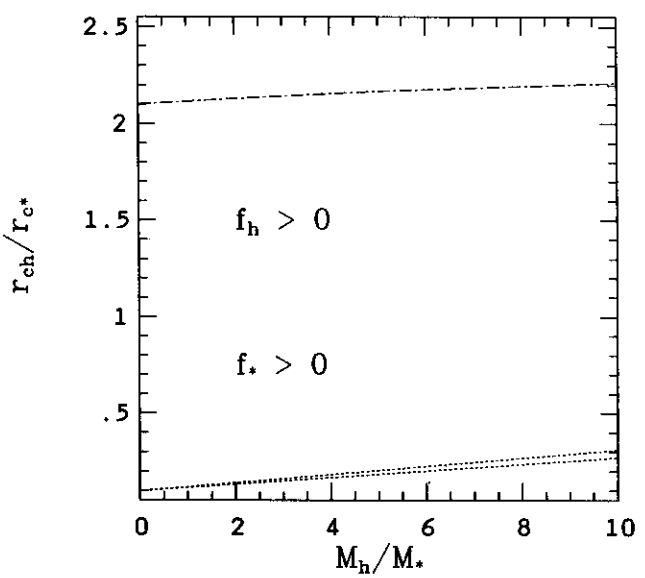

Figure 5. The region of consistency for KGs. The dot-dashed line marks the upper boundary of the region of DH consistency, and is independent of r_{ah}. The dotted lines mark the lower boundary for the stellar component consistency; the lower one refers to $r_{a*}=\infty$, the higher to $r_{a*}=0.1r_{c*}$.

© Royal Astronomical Society • Provided by the NASA Astrophysics Data System

As for KGs, there is a lower limit on R_{ch}/R_{c*} for the consistency of the dVGs' stellar component, but it lies well below $R_{ch}=0.2R_{c*}$, varying M_h from 0 to $10M_*$, and for $r_{a*}\geq 0.1R_{c*}$; the DH consistency is assured until very large values of R_{ch}/R_{c*}, for $r_{ah}\geq 0.1R_{ch}$. So, thanks to the same behaviour of the stars and of the DH mass distribution, a large range of values for the characteristic dVGs' parameters is permitted.

5 MASS ESTIMATORS

The determination of the total and the stellar masses of ellipticals cannot be separated from the determination of their internal dynamics and intrinsic shape. If these are available, the kinematics of a set of tracer objects can be used to find the gravitational potential, and then the density distribution which generates it. Practically, much of this information is left unknown by the observations, so methods of calculating masses make use of approximations. For example, the two standard approaches to the problem of determining the mass-to-light ratio, the core-fitting method (Richstone & Tremaine 1986) and the virial method (Binney 1982), produce a value of M_*/L_B based on kinematic observations inside R_{c*}, and on the hypothesis of stellar isotropic orbits. Here we want to consider various commonly used *mass estimators*, and we show how their results deviate from the true values of the total and stellar galaxy masses, due to the presence of the DH and the velocity anisotropy.

If one observes $I(R)$ and $\sigma_p^2(R)$ of an elliptical galaxy, and assumes its M_*/L_B to be constant, one can use an isotropic mass estimator:

$$M_E = K_*^I E(\sigma_p^2, I), \tag{12}$$

where E depends only on observationally accessible quantities. The dimensionless factor K_*^I is uniquely determined for any $\rho_*(r)$, assuming isotropic velocity dispersion, no DH and a specific form for E. The value recovered from (12) won't necessarily be the true total mass value, which is:

$$M_T = K_T E(\sigma_p^2, I), \tag{13}$$

where E is the same function as in (12); for example $K_T = K_T(M_h/M_*, r_{ch}/r_{c*}, r_t/r_{c*}, r_{a*}/r_{c*})$ in the case of KGs. M_E is different from M_* and from M_T, if anisotropy and dark matter are present in the galaxy, and from (12) and (13) we recover

$$\frac{M_E}{M_*} = \frac{1+M_h/M_*}{K_T/K_*^I}. \tag{14}$$

If we choose E so that the right member of (14) turns out to be nearly constant, *independently* of the parameters' values, this E can be considered to provide a good stellar mass estimate (since we know what error we make on the estimate of M_*), but a bad total mass estimate. From (14) one easily derives also the deviation of M_E/L_B relative to M_*/L_B. This is useful in order to obtain some indications of the presence of DH and/or velocity dispersion anisotropy, in case one has some clues about the value of M_*/L_B.

For KGs, we study an E function of the form:

$$E(\sigma_p^2, I_K) = \frac{r_{c*}\sigma_p^2(0)}{G}. \tag{15}$$

Table 1. The dimensionless parameter K_*^I of KGs.

r_t/r_{c*}	K_*^I
140	41.689
160	42.890
180	43.950
200	44.898
220	45.756

In Table 1 we give the values of K_*^I when (15) is in cgs units, for various r_t/r_{c*}.

While in KGs the velocity dispersion profile is flat in the central regions of the galaxy, for dVGs this is not the case, and so the problem arises of finding a well-defined quantity with which to perform our calculations. Following Bailey & MacDonald (1981) we use $\sigma_a^2(R)$, i.e. $\sigma_p^2(R)$ weighted with $I(R)$ over a circular aperture of radius R centred on the galaxy. In practice, measured velocity dispersions are always averaged over a finite central region of radius at least as great as the seeing disc, and sometimes much larger. So, we consider two different E functions:

$$E(\sigma_p^2, I_{dV}) = \frac{R_{c*}\sigma_a^2(0.1R_{c*})}{G} \tag{16}$$

and

$$E(\sigma_p^2, I_{dV}) = \frac{R_{c*}\sigma_a^2(R_{c*})}{G}. \tag{17}$$

We derive for K_*^I the values 4.471 and 5.775 respectively, using (16) and (17) in cgs units. Summarizing, for our models the estimated mass can be recovered from the following formula:

$$M_E = 233.2 \begin{cases} K_*^I r_{c*}\sigma_p^2(0), \\ K_*^I R_{c*}\sigma_a^2(0.1R_{c*}), \\ K_*^I R_{c*}\sigma_a^2(R_{c*}), \end{cases} \tag{18}$$

where the K_*^I are those given in the text, M_E is in solar masses, the radii are in parsecs, and the velocity dispersions are in km s^{-1}. It is also interesting to check whether $0.5M_E$ can be a good estimator of the total mass contained within the cylinder of radius R_{c*}, M_{cT}. Using the above calculations we can write:

$$\frac{0.5M_E}{M_{cT}} = \frac{1+M_h/M_*}{K_T/K_*^I}\left[1+\frac{2M_h(R_{c*})}{M_*}\right]^{-1}. \tag{19}$$

5.1 Exploring the parameter space

In this paragraph we discuss the behaviour of M_E/M_* and of $M_{cT}/0.5M_E$. The parameter space for KGs is explored as follows: $(M_h/M_*, r_{ch}/r_{c*}, r_{a*}/r_{c*})$ vary in the cube $[0, 10]\times[0.1, 2.5]\times[1.2, \infty[$, and $r_t = 140r_{c*}$. For dVGs, $(M_h/M_*, R_{ch}/R_{c*}, r_{a*}/R_{c*})$ vary in the cube $[0, 10]\times[0.1, 4]\times[0.1, \infty[$, and $r_t = 15R_{c*}$. For each cube a three-dimensional grid of $21\times21\times4$ models has been computed. Good fits (within 5 per cent) of the values found for M_E/M_* are given by:

© Royal Astronomical Society • Provided by the NASA Astrophysics Data System

$$\frac{M_E}{M_*} \simeq \frac{3.835+(r_{a*}/r_{c*})^2}{0.936+(r_{a*}/r_{c*})^2}\left[1+0.044\,\frac{M_h}{M_*}\left(\frac{r_{ch}}{r_{c*}}\right)^{-0.82}\right], \qquad (20)$$

for the E function in (15),

$$\frac{M_E}{M_*} \simeq \frac{0.077+(r_{a*}/R_{e*})^2}{0.033+(r_{a*}/R_{e*})^2}\left[1+0.95\,\frac{M_h}{M_*}\left(\frac{R_{eh}}{R_{e*}}\right)^{-1.04}\right], \qquad (21)$$

for that in (16) and

$$\frac{M_E}{M_*} \simeq \frac{1.475+(r_{a*}/R_{e*})^2}{1.252+(r_{a*}/R_{e*})^2}\left[1+0.93\,\frac{M_h}{M_*}\left(\frac{R_{eh}}{R_{e*}}\right)^{-0.73}\right], \qquad (22)$$

for that in (17).

The value of M_E/M_* for $M_h = 0$ is the measure of the error induced only by the presence of the stellar anisotropy on the estimate of the stellar mass. Changing r_{a*} from the isotropic case down to $0.5R_{e*}$ (or $6r_{c*}$), this error varies from 0 to ~15 per cent. So (15), (16) and (17) are quite good stellar mass estimators, if no DH is present. Note that a plausible value of r_{a*} in the dissipationless scenario of galaxy formation is $r_{a*} \approx R_{e*}$ (e.g. Bertin *et al.* 1991). For $r_{a*} < 0.5R_{e*}$, only (17) still gives good M_* estimates, because integrating $\sigma_p^2(R)$ over a larger portion of the galaxy is nearer to the validity conditions of the virial projection theorem of Kent (1990). On the contrary, (15) and (16) give errors larger than 50 per cent.

If a DH is present, the stellar mass estimates obtained for KGs are generally much better than those for dVGs, which are completely wrong if $M_h > M_*$. This is due to the much larger amount of dark matter in the central regions of dVGs (see Fig. 2), and also to averaging over a larger region of the galaxy, using (16) and (17) instead of (15). In Fig. 6 we show the behaviour of M_*/M_E as a function of M_h/M_*, for three values of r_{a*} and two fixed values of the characteristic radii ratio. All the features described above are apparent.

In Fig. 7 we show the ratio $M_{eT}/0.5M_E$ as a function of M_h/M_*, for the same set of parameters as in Fig. 6. We see that in this case the estimated mass within the effective radius can be larger or smaller than the total mass within the same radius. So, estimated M_E/L_B are systematically larger than or equal to M_*/L_B, while $0.5M_E/L_B$ can be less or larger than M_{eT}/L_B. The right-most panel shows how quite good estimates of the total mass within the effective radius can be obtained when averaging the stellar velocity dispersion over a larger fraction of the galaxy.

6 TWO APPLICATIONS

6.1 The models on the fundamental plane

Djorgovski & Davis (1987) and Dressler *et al.* (1987) have shown that the manifold of ellipticals populate a planar distribution in a three-dimensional parameter space of observable quantities: a linear combination of $\log \sigma$ and $\log I$ (I is the mean surface brightness within R_{e*}) with $\log R_{e*}$, or $\log L_B$, produces excellent fits of this manifold, called *fundamental planes*. A fundamental plane can be used together with (12) and (14) to connect observable quantities with the structural, unobservable parameters of ellipticals. Taking the observed L_B from the fundamental plane $R_{e*} \sim \sigma^A I^B$, we derive

$$\frac{K_T(M_*/L_B)^{-1}}{1+M_h/M_*} \propto \sigma^{-2-A/B} R_{e*}^{1+1/B}, \qquad (23)$$

where the constant of proportionality is fixed by the observations. Equation (23) relates a two-dimensional space of observables (R_{e*}, σ) to the structural space of the parameters. Each curve $\sigma^{-2-A/B} R_{e*}^{1+1/B} = constant$ corresponds to a hypersurface in the structural space, and different values of the constant correspond to distinct (non-intersecting) hypersurfaces. It is possible that the shape and the relative displacement of these hypersurfaces contain important statistical connections of the structural properties of ellipticals with their observable quantities.

6.2 Energetics of a hot gas component

Einstein's X-ray observations have shown that brighter ellipticals contain large quantities of hot gas, produced by the

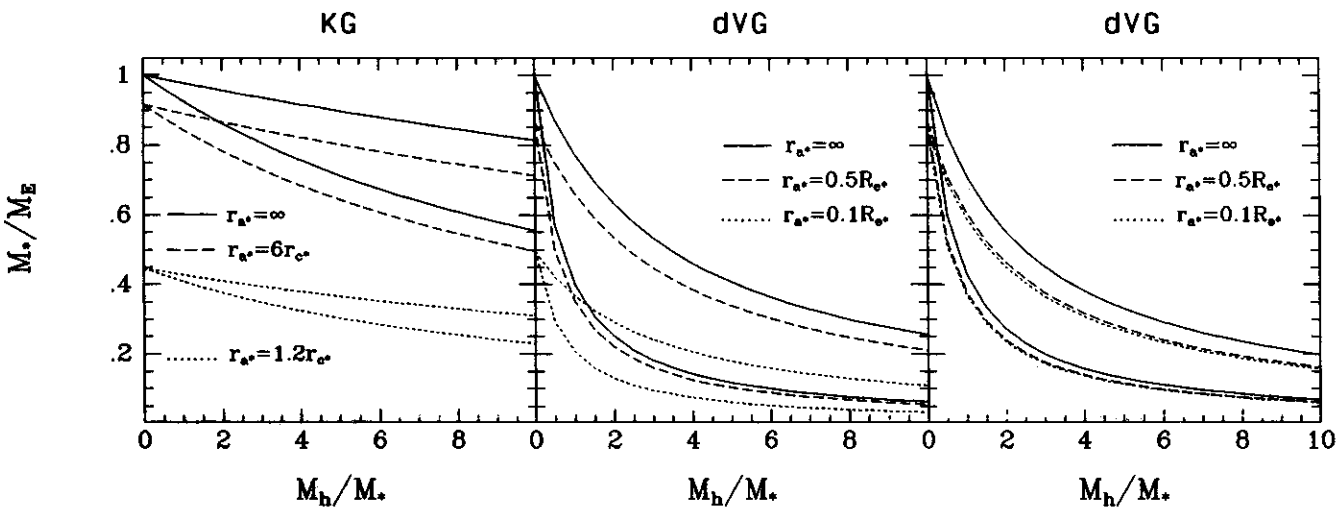

Figure 6. M_*/M_E as a function of M_h/M_*. For each r_{a*}, the two curves correspond to $r_{ch} = 0.6r_{c*}$ (lower curve) and to $r_{ch} = 2r_{c*}$, for KGs; to $R_{eh} = 0.7R_{e*}$ (lower curve) and to $R_{eh} = 3R_{e*}$ for dVGs. The central dVG panel shows the results of using the estimator in (16), while the right-most panel refers to that in (17).

© Royal Astronomical Society • Provided by the NASA Astrophysics Data System

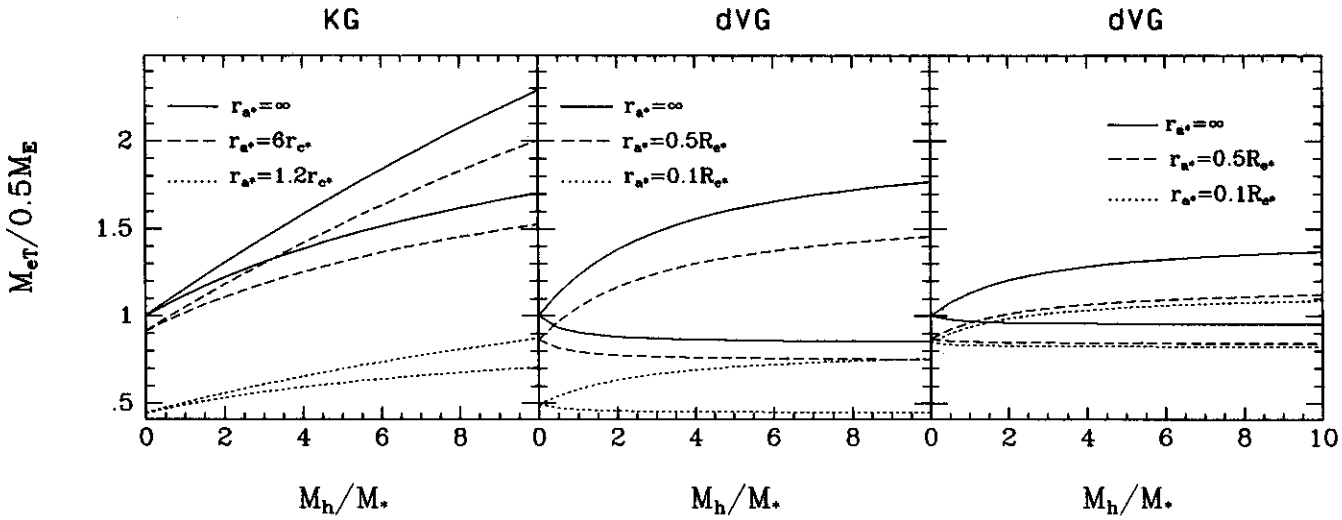

Figure 7. $M_{cT}/0.5M_E$ as a function of M_h/M_*. For each r_{a*}, the two curves correspond to $r_{ch}=0.6r_{c*}$ (lower curve) and to $r_{ch}=2r_{c*}$, for KGs; to $R_{ch}=0.7R_{e*}$ (lower curve) and to $R_{ch}=3R_{e*}$ for dVGs. The central dVG panel shows the results of using the estimator in (16), while the rightmost panel refers to that in (17).

stellar mass loss during a Hubble time (e.g. Canizares, Fabbiano & Trinchieri 1987). The main observed characteristics of this X-ray emission can be explained with hydrodynamical simulations of the evolutionary behaviour of this gas (see Ciotti *et al.* 1991 and references therein). This treatment needs as main physical ingredients two quantities related to the depth of the galaxies' potential well, and the heating of the stellar mass loss by thermalization of the stellar velocities (stellar heating). The first two ingredients are $L^-_{grav}(r)$, defined as the power required to remove steadily and bring to infinity the gas shed by stars within the radius r in unit time, and $L^+_{grav}(r)$, the power generated by the steady inflow of this gas through the galactic potential well, down to the centre of the galaxy. Thus we have:

$$L^-_{grav}(r)=-\frac{\dot M_*(t)}{M_*}\int_0^r 4\pi r^2\rho_*(r)\,\phi(r)\,dr \tag{24}$$

and

$$L^+_{grav}(r)=\frac{\dot M_*(t)}{M_*}\int_0^r 4\pi r^2\rho_*(r)[\phi(r)-\phi(0)]\,dr, \tag{25}$$

where $\dot M_*(t)/M_*$ is the specific rate of stellar mass return (Ciotti *et al.* 1991). The integrals appearing in these definitions can be expressed as products of three terms: the mass loss rate, a measure of the depth of the stellar potential well, and a dimensionless form factor. So, for KGs, we have

$$L^\pm_{grav}(r)=\dot M_*(t)\frac{GM_*}{r_{c*}}\,U^\pm_*(r/r_{c*}), \tag{26}$$

where $U^\pm_*(r/r_{c*})$ depends on M_h/M_*, r_{ch}/r_{c*}, r_t/r_{c*}, and its explicit form can be recovered after some tiresome algebra. The third physical quantity connected with the X-ray emission of ellipticals is the stellar heating $L_\sigma(r)$:

$$L_\sigma(r)=\frac{1}{2}\,\frac{\dot M_*(t)}{M_*}\int_0^r 4\pi r^2\rho_*(r)\,\sigma^2(r)\,dr. \tag{27}$$

Following the same reasoning as for $L^\pm_{grav}$, we write for KGs:

$$L_\sigma(r)=\dot M_*(t)\frac{GM_*}{r_{c*}}\,T_*(r/r_{c*}). \tag{28}$$

The dimensionless function $T_*(r/r_{c*})$ depends also on r_{a*}/r_{c*}. In the particular case of $r=r_t$, the dependence on r_{a*} vanishes, as can be demonstrated for any $\rho_*(r)$ and for a *general* $\alpha_*(r)$. In fact, a useful formula for $L_\sigma(r)$ can be easily derived, using $\sigma^2(r)=[3-2\alpha_*(r)]\,\sigma_r^2(r)$, recovering $\alpha_*(r)$ from (7), and inserting this expression in (27); after an integration by parts:

$$\frac{L_\sigma(r)M_*}{2\pi G\dot M_*(t)}=\int_0^r r\rho_*(r)[M_*(r)+M_h(r)]\,dr+r^3\rho_*(r)\,\sigma_r^2(r), \tag{29}$$

that is clearly *independent* of any anisotropy distribution for the stellar component if $r=r_t$. While the quantities introduced in (26) and (28) singularly depend on M_*, with all the related uncertainties, the ratio $L^\pm_{grav}(r)/L_\sigma(r)$ is exempt from this problem.

In Fig. 8 we show the behaviour with respect to M_h/M_* of $U^\pm_*$, T_* and of the ratio U^-_*/T_*, all calculated in r_t. The trend of $U^\pm_*$ and T_* with M_h is obviously linear. At any fixed M_h/M_*, U^+_* is more sensitive to the DH concentration than U^-_*, because in extracting the gas from its birthplace to infinity, what counts is essentially the total mass of the galaxy, while the energy released falling in depends strongly on the particular shape of the potential well. The ratio U^-_*/T_* is 4 if $M_h=0$, for the virial theorem, and tends to a constant value for $M_h\to\infty$.

7 CONCLUSIONS

King and de Vaucouleurs spherical galaxy models, embedded in a dark matter halo, are examined, assuming the stellar mass-to-light ratio is constant. The radial behaviour of the velocity dispersion tensor of each component satisfies the

© Royal Astronomical Society • Provided by the NASA Astrophysics Data System

relation $\sigma_\theta^2(r)/\sigma_r^2(r) = r_a^2/(r^2+r_a^2)$. The main results are summarized as follows.

(i) The main features of the velocity dispersion profiles of KGs are that the DH assumed makes the isotropic profiles quite flat, and that the stellar anisotropy may increase the velocity dispersion in the central regions of the galaxy as much as a massive DH. In dVGs both these effects are absent: the profiles are always bell-shaped (more peaked for a higher DH concentration), and the action of the DH is always prevalent on that of the anisotropy, if $M_h > M_*$. Moreover, for both dVGs and KGs, the drop of the velocity dispersion at large radii cannot exclude the presence of a massive DH.

(ii) The self-consistency of our models has been investigated numerically and with the aid of a theorem enlightening the various roles of the density profile and the velocity dispersion anisotropy in determining the consistency of each component of a collisionless spherical system.

With our particular choice of the radial trend of the anisotropy, de Vaucouleurs stellar profiles cannot be consistently coupled to quite flat density distributions, such as a quasi-isothermal dark halo. In fact, the distribution function of the halo, f_h, turns out to be negative if $r_{ch} \geq 10^{-3} R_{e*}$. This result holds also when the dark halo velocity dispersion tensor is isotropic.

KGs are self-consistently generated roughly for $0.3 r_{c*} < r_{ch} < 2.2 r_{c*}$, if $0 < M_h \leq 10 M_*$ and provided that $r_{a*} > 0.896 r_{c*}$. The lower limit on r_{ch}/r_{c*} is required for the stellar component consistency, the upper limit for the DH component consistency, and is independent of r_{ah}. dVGs are self-consistently generated in the parameter space $0 \leq M_h \leq 10 M_*$, $R_{eh} \geq 0.2 R_{e*}$, for $r_{a*} \gtrsim 0.1 R_{e*}$, thanks to the fact that in this case the DH and the stars' density profiles have the same shape.

(iii) Velocity dispersion profiles integrated over apertures and inserted in the most common mass estimators give stellar masses which can be extremely uncertain. For KGs, if the velocity dispersion is highly anisotropic, the errors can be comparable to those determined by the presence of a massive dark halo in isotropic models. Estimates in the dVG case may be completely wrong if $M_h > M_*$. The estimate of the total mass within the effective radius is quite accurate if one uses velocity dispersions averaged with the luminosity profile out to one effective radius. In any case, the estimated mass-to-light ratios are always larger than M_*/L_B, while the

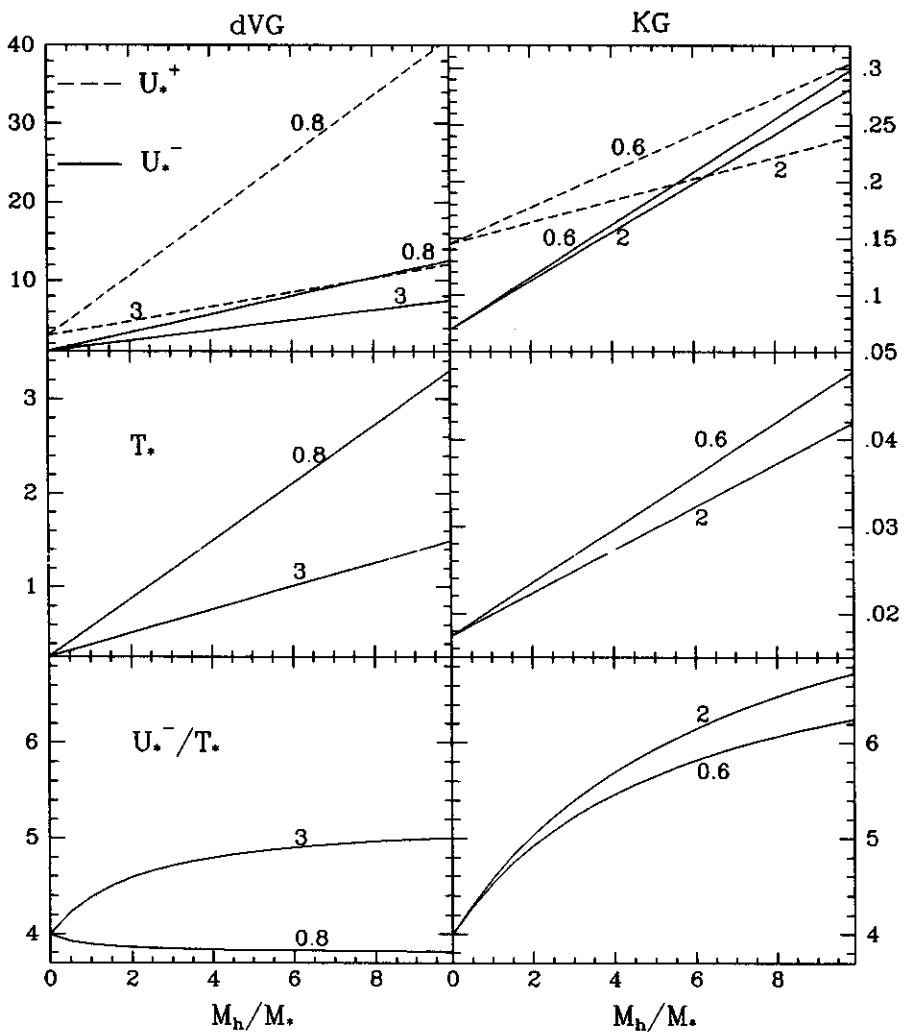

Figure 8. The functions U_*^+ (dashed lines), U_*^- (solid lines), T_* and U_*^-/T_* evaluated in r_t as functions of M_h/M_*, for KGs (right panels) and dVGs (left panels). The numbers on each curve show the values of r_{ch}/r_{c*} and of R_{eh}/R_{e*}.

© Royal Astronomical Society • Provided by the NASA Astrophysics Data System

estimated mass-to-light ratios inside R_{e*} can be larger or smaller than the true value.

ACKNOWLEDGMENTS

We wish to thank G. Bertin, A. D'Ercole, E. Held, A. Renzini, M. Stiavelli and P. Cuddeford for useful discussions and suggestions. We warmly thank the referee, P. L. Palmer, whose suggestions have improved the paper. This work has been partially supported by the Italian Ministry of Research (MURST).

REFERENCES

Bailey, M. E. & MacDonald, J., 1981. *Mon. Not. R. astr. Soc.*, **194**, 195.
Bertin, G. & Stiavelli, M., 1984. *Astr. Astrophys.*, **137**, 26.
Bertin, G., Saglia, P. & Stiavelli, M., 1991. Preprint.
Bertin, G., Bertola, F., Buson, L., Danziger, J., Dejonghe, H., Sadler, E., Saglia, P., Vietri, M., de Zeeuw, P. T. & Zeilinger, W., 1989. *The Messenger*, **56**, 19.
Bertola, F., Bettoni, D., Danziger, J., Sadler, E., Sparke, L. & de Zeeuw, T., 1991. *Astrophys. J.*, **369**, 390.
Binney, J., 1980. *Mon. Not. R. astr. Soc.*, **190**, 873.
Binney, J., 1982. *Ann. Rev. Astr. Astrophys.*, **20**, 399.
Binney, J. & Mamon, G. A., 1982. *Mon. Not. R. astr. Soc.*, **200**, 361.
Binney, J. & Tremaine, S., 1987. *Galactic Dynamics*, Princeton University Press, Princeton (BT87).
Canizares, C. R., Fabbiano, G. & Trinchieri, G., 1987. *Astrophys. J.*, **312**, 503.
Ciotti, L., D'Ercole, A., Pellegrini, S. & Renzini, A., 1991. *Astrophys. J.*, **376**, 380.
de Vaucouleurs, G., 1948. *Ann. d'Astrophys.*, **11**, 247.
Djorgovski, S. & Davis, M., 1987. *Astrophys. J.*, **313**, 59.
Dressler, A., Lynden-Bell, D., Burstein, D., Davies, R. L., Faber, S. M., Terlevich, R. J. & Wegner, G., 1987. *Astrophys. J.*, **313**, 42.
Forman, W., Jones, C. & Tucker, W., 1985. *Astrophys. J.*, **293**, 102.
Kent, S. M., 1990. *Mon. Not. R. astr. Soc.*, **247**, 702.
King, I., 1962. *Astr. J.*, **67**, 471.
King, I., 1966. *Astr. J.*, **71**, 64.
King, I., 1972. *Astrophys. J. Lett.*, **174**, L123.
Kormendy, J., 1987. In: *Structure and Dynamics of Elliptical Galaxies*, p. 17, ed. de Zeeuw, T., Reidel, Dordrecht.
Lees, J. F., van Gorkom, J. H. & Knapp, G. R., 1990. *Bull. Am. astr. Soc.*, **21**, 1178.
Mathews, W. G., 1988. *Astr. J.*, **95**, 1047.
Mellier, Y. & Mathez, G., 1987. *Astr. Astrophys.*, **175**, 1.
Merritt, D., 1985. *Astr. J.*, **90**, 1027.
Merritt, D., 1988. *Astr. J.*, **95**, 496.
Poveda, A., 1958. *Bol. Obs. Tonantzintla, No. 17*, 3.
Richstone, D. O. & Tremaine, S., 1984. *Astrophys. J.*, **286**, 27.
Richstone, D. O. & Tremaine, S., 1986. *Astr. J.*, **92**, 72.
Tonry, J. L., 1983. *Astrophys. J.*, **266**, 58.
van Albada, T. S., 1982. *Mon. Not. R. astr. Soc.*, **201**, 939.
Young, P. J., 1976. *Astr. J.*, **81**, 807.

© Royal Astronomical Society • Provided by the NASA Astrophysics Data System